Metabolic modelling identifies mitochondrial Pi uptake and pyruvate efflux as key aspects of daytime metabolism and proton homeostasis in crassulacean acid metabolism leaves

Metabolic modelling identifies mitochondrial Pi uptake and pyruvate efflux as key aspects of day-time metabolism and proton homeostasis in CAM leaves

Stijn Daems[a,b], Sanu Shameer[c,d], Nathalie Ceusters[a], Lee Sweetlove[c] and Johan Ceusters[a,b,e,1]

[a]Research Group for Sustainable Crop Production & Protection, Division of Crop Biotechnics, Department of Biosystems, KU Leuven, Geel, Belgium

[b]KU Leuven Plant Institute (LPI), KU Leuven, Leuven, Belgium

[c]Department of Biology, University of Oxford, Oxford OX1 3RB, United Kingdom

[d]Indian Institute of Science Education and Research Thiruvananthapuram, Kerala 695551, India

[e]Centre for Environmental Sciences, Environmental Biology, UHasselt, Diepenbeek, Belgium

[1] **Correspondence:**

Johan Ceusters

johan.ceusters@kuleuven.be

ORCIDs:

Stijn Daems: 0000-0002-7459-7765

Sanu Shameer: 0000-0002-0227-4422

Nathalie Ceusters: 0000-0002-8374-0447

Lee Sweetlove: 0000-0002-2461-4133

Johan Ceusters: 0000-0002-5225-9159

Word counts: Introduction: 1280; Materials and Methods: 1375; Results: 1912; Discussion: 1831

Total word count: 6398

Number of Figures: 6 (all in colour)

Number of Tables: 0

Number of Supporting Information files: 34 (Figs S1-S8, Tables S1-S20, Methods S1, Notes S1-S5; all combined in two files: SI Word-file + SI Excel-file)

Summary

- Crassulacean acid metabolism (CAM) leaves are characterized by nocturnal acidification and diurnal deacidification processes related with the timed actions of phospho*enol*pyruvate carboxylase and Rubisco respectively. How CAM leaves manage cytosolic proton homeostasis, particularly when facing massive diurnal proton effluxes from the vacuole, remains unclear.
- A 12-phase flux balance analysis (FBA) model was constructed for a mature malic enzyme-type CAM mesophyll cell in order to predict diel kinetics of intracellular proton fluxes.
- The charge- and proton-balanced FBA model identified the mitochondrial phosphate carrier (PiC, Pi/H^+ symport), which provides Pi to the matrix to sustain ATP biosynthesis, as a major consumer of cytosolic protons during day-time (>50%). The delivery of Pi to the mitochondrion, co-transported with protons, is required for oxidative phosphorylation and allows sufficient ATP to be synthesized to meet the high energy demand during CAM Phase III. Additionally, the model predicts that mitochondrial pyruvate originating from decarboxylation of malate is exclusively exported to the cytosol, probably via a pyruvate channel mechanism, to fuel gluconeogenesis. In this biochemical cycle, glyceraldehyde 3-phosphate dehydrogenase (GAPDH) acts as another important cytosolic proton consumer.
- Overall, our findings emphasize the importance of mitochondria in CAM and uncover a hitherto unappreciated role in metabolic proton homeostasis.

Key words: CAM mitochondria, crassulacean acid metabolism (CAM), diurnal deacidification, flux balance analysis modelling, malic enzyme-type CAM leaf, metabolic proton homeostasis, mitochondrial phosphate carrier (PiC), vacuolar proton efflux

Introduction

Crassulacean acid metabolism (CAM) species reschedule all, or a part of photosynthetic CO_2 uptake from day to night, which results in substantially improved water-use efficiency (WUE) (Borland *et al*., 2009). During CAM Phase I, nocturnal opening of stomata allows atmospheric CO_2 to be converted to bicarbonate (HCO_3^-) by carbonic anhydrase (CA) which is subsequently fixed into organic carbon by phospho*enol*pyruvate carboxylase (PEPC). The product, oxaloacetate, is converted to malate by malate dehydrogenase and is stored in the vacuole accompanied with protons being pumped in by a dedicated tonoplast H^+ V-ATPase and/or H^+-PP_iase, which causes a substantial night-time vacuolar acidification up to about pH 3 (Lüttge & Smith, 1984; Franco *et al*., 1990). These proton fluxes provide charge balance for the accumulated malate and also act to preserve cytosolic pH within physiological bounds during the night (Osmond, 1978; Bartholomew *et al*., 1996; Tsiantis *et al*, 1996; Borland *et al*., 2011; Winter & Smith, 2022).

During the day, malate is remobilized from the vacuole and decarboxylated to supply ribulose 1,5-bisphosphate carboxylase/oxygenase (Rubisco) with CO_2 behind closed stomata (Phase III). This phase is particularly energy demanding, constituting both the Calvin-Benson-Bassham (CBB) cycle and the gluconeogenic recovery of (phospho*enol*)pyruvate to the level of storage carbohydrate (Winter & Smith, 1996; Schöttler *et al*., 2002). Decarboxylation is mediated by mitochondrial NAD-malic enzyme (ME) and/or cytosolic/chloroplastic NADP-ME (ME-type plants), or cytosolic phospho*enol*pyruvate carboxykinase (PEPCK; PEPCK-type plants; Dittrich *et al*., 1973; Dittrich, 1976; Holtum *et al*., 2005), depending on the CAM species. For NAD-ME species in particular the fate of the liberated pyruvate inside the mitochondrion remains unclear. Holtum & Osmond (1981) suggested that NAD-ME-generated pyruvate is not oxidized to CO_2 in the tricarboxylic acid (TCA) cycle, but rather quantitively converted to PEP via pyruvate orthophosphate dikinase (PPDK) in the cytosol, in order to conserve the 3-C residue in gluconeogenesis. As recent findings by Le *et al.* (2021) indicate that the mitochondrial pyruvate carrier (MPC) in plants is only able to import pyruvate into mitochondria, the identity and working mechanism of the plant mitochondrial pyruvate exporter is currently unknown. The two major CAM phases (I and III) are flanked by two intermediate phases II and IV, at the onset

and end of the day when stomata gradually close and reopen respectively, in which CO_2 is fixed by combined action of both PEPC and Rubisco (Osmond, 1978; Borland *et al*., 2011).

The diurnal release of malate from the vacuole is accompanied by net proton export to the cytosol and subsequent processing of these protons, which is consistent with the characteristic increase in leaf sap pH of CAM species (Osmond, 1978; Hafke *et al*., 2001). For the majority of the day, vacuolar efflux primarily occurs as $Hmalate^-$ and/or $malate^{2-}$, and a substantial body of evidence gathered in the past indicates an intimate stoichiometry of $2H^+$:$malate^{2-}$ (or alternatively $1H^+$:$Hmalate^-$). Whilst the diurnal fate of malate has been characterized at the biochemical level, the intracellular proton fluxes in a CAM leaf have received considerably less scrutiny (Ceusters *et al*., 2021). Due to its relatively small volume (about 0.5-1% of the total cell volume) in comparison to the vacuole, the cytosol of CAM mesophyll cells is especially prone to over-acidification (Rona *et al*., 1980; Steudle *et al*., 1980; Smith & Heuer, 1981). Cytosolic pH homeostasis is extremely important to safeguard the functionality of the cytosol as an important transit compartment for many solutes and as medium to accommodate different important biochemical pathways such as gluconeogenesis and sucrose biosynthesis. By monitoring day-to-night vacuolar and cytosolic pH changes in protoplasts of the CAM plant *Kalanchoë daigremontiana*, Hafke *et al*. (2001) reported a steep increase in vacuolar pH (from ca. pH 4 to 5) during the first half of the day owing to a strong decline in vacuolar malate (from ca. 300 to 100 mM) and concomitant H^+ concentration. However, only relatively minor changes in cytosolic pH (0.34 units) were observed, illustrating the tight control of cytosolic pH to secure diurnal proton homeostasis in CAM mesophyll cells (Lüttge *et al*., 1982; Marigo *et al*., 1983; Hafke *et al*., 2001).

Besides its importance in CO_2 sequestration for CAM species, ME has also been assigned a general, essential function in cellular pH homeostasis (biochemical pH-stat) (Davies, 1986; Sakano, 1998). Acid-induced decarboxylation of malate liberates NADH and its subsequent respiratory oxidation acts to elevate cellular pH levels by direct proton consumption when molecular oxygen is reduced to water at the end of the mitochondrial electron transport chain (mETC) (Sakano, 1998). Rapid cytosolic acidification (i.e. within seconds to minutes) has been noticed in C_3 and C_4 plant cells under hypoxic or anoxic conditions, or when the mETC is pharmacologically inhibited (Roberts *et al*., 1982, 1984; Felle, 2005; Wagner *et al*., 2019). These

observations indicate that the primary cause for cytosolic acidification during O_2 depletion is likely the inhibition of electron transport activity, suggesting a crucial role for the mETC in cellular pH homeostasis.

To shed more light on the mechanisms in cellular pH homeostasis, a comprehensive and quantitative analysis of all biochemical reactions involving protons is required. Although dynamic models of CAM have been developed over the years (Owen & Griffiths, 2013; Wang *et al.*, 2023), they lack the adequate representation of proton fluxes needed for such an analysis. To envisage these fluxes in large metabolic networks, such as leaf mesophyll cells, flux balance analysis (FBA) has emerged as a useful computational modelling tool (Sweetlove & Ratcliffe, 2011; Chomthong & Griffiths, 2020). FBA can make accurate predictions of reaction fluxes in large metabolic networks by interrogating an n-dimensional solution space formulated from a system of linear equations that each represent the relationship between the stoichiometry of a reaction and its flux at steady state. The solution space is typically constrained by the underlying biophysics and thermodynamics of the system as well as by experimental measures of metabolic inputs and outputs (Clark *et al.*, 2020). Although this modelling framework does not directly account for regulatory features of the system, for example the response to changes in metabolite and effector concentrations, it nevertheless provides flux predictions that are remarkably accurate given the relatively simple modelling formulation (Williams *et al*., 2010; Kaste & Shachar-Hill, 2023). The advantage of the relatively simple modelling formulation is that it can be scaled up to capture very large systems of reactions, which is essential for capturing the fluxes of protons which are involved in very many reactions and transport processes. Moreover, although formally a steady-state framework, the steady state assumption can be relaxed for specified metabolites, allowing the dynamics of accumulation and consumption of metabolites over the CAM cycle to be captured. Several flux balance models have already explored CAM photosynthesis to some extent, ranging from two-phase day-night models, to 24-h models with a 1-h time resolution (Cheung *et al*., 2014; Shameer *et al*., 2018; Töpfer *et al*., 2020; Tay *et al*., 2021). Based on a formerly built two-phase day-night CAM model, an initial exploration of possible intracellular proton flows highlighted a putative key role for mitochondria to relieve the cytosol from its diurnal 'proton pressure' (Shameer *et al*., 2018). However, mitochondria have only received marginal attention so far in CAM research (Leverett & Borland, 2023) and the exact identities of different mitochondrial transporters still need to be established.

Here, we develop a diel flux balance analysis model of CAM leaf metabolism on a 2-h basis resolution (12-phase model) guided by an experimental dataset of gas exchange and diel metabolite time courses in a ME-type CAM leaf (Ceusters *et al*., 2019). This model is used to address the following questions related to the diurnal process of CAM. (i) How are CAM leaves able to metabolically secure cytosolic proton homeostasis? (ii) What is the fate of NAD-ME-derived pyruvate?

Materials and Methods

Model description - Development of a 12-phase malic enzyme-type CAM leaf metabolic modelling framework

A previously-published diel-FBA framework (Cheung *et al*., 2014) approach was expanded upon to develop a stoichiometric model of malic enzyme (ME)-type CAM leaves with 12 temporal phases (i.e. each interval represents 2 hours of the diel cycle), similar to the 24-phase model by Töpfer *et al*. (2020), by concatenating 12 copies of PlantCoreMetabolism v2.0, a charge- and proton-balanced diel-FBA model of plant primary metabolism (Shameer *et al*., 2022). Identifiers (IDs) of reactions, metabolites and compartments corresponding to each temporal phase were suffixed with the respective temporal phase number (Ex: ID for GLC_c in temporal phase 5 is changed to GLC_c5). To establish the model for a single diel cycle, a light input of 100 μmol m^{-2} s^{-1} was defined for a 12-h light period. Leaf non-growth associated maintenance (NGAM) costs, represented in the model using ATP hydrolysis and NADPH oxidase reactions, were estimated based on the incident light and imposed as described in Töpfer *et al*. (2020).

The four CAM phases of gas exchange (CAM phases I, II, III, and IV) were integrated into the modelling framework by constraining CO_2 exchange between the CAM leaf and the environment. During phase I (night) and phases II and IV (intermediate phases) the model was only allowed to take up CO_2, whilst in phase III (day) the model was only allowed to emit CO_2 (Fig. 1). More specifically, CO_2 exchange fluxes were constrained for (a) uptake with a maximum flux of 3.3 μmol m^{-2} s^{-1} for temporal phases 7-12 (CAM Phase I), (b) uptake with a maximum flux of 1.2 μmol m^{-2} s^{-1} for temporal phase 1 (CAM Phase II), (c) no uptake for

temporal phases 2-5 (CAM Phase III) and (d) uptake with a maximum flux of 0.9 μmol m^{-2} s^{-1} for temporal phase 6 (CAM Phase IV), consistent with gas exchange measurements in *Phalaenopsis* 'Edessa' (Ceusters *et al*., 2019) (Fig. S1, Table S1). Fig. S2 shows the resulting model predictions for the diel course of different key metabolites (starch, malate, sucrose, and citrate).

The carboxylic acids (malate, citrate, and isocitrate), the sugars (glucose, fructose, and sucrose), and starch were identified as metabolites that accumulate to significant levels (i.e. micromoles g^{-1}FW) in ME-type CAM leaves over the diel cycle based on Ceusters *et al.* (2019). To facilitate such transient accumulations in the CAM leaf model, linker reactions that transfer these metabolites from one temporal phase to the next (representing accumulation fluxes of metabolites across temporal phases) were added to the vacuole (for malate, citrate, isocitrate, glucose, fructose, and sucrose) and plastid (for starch). Similar linker reactions were also added to permit vacuolar proton accumulation between temporal phases in order to account for the acidification and deacidification of CAM leaves during the night and day respectively. These linker reactions were given IDs based on the metabolites and the temporal phases involved (Ex: STARCH_p accumulating between temporal phase 3 and 4 is represented by reaction ID STARCH_p3_accumulation). Data from *Phalaenopsis* 'Edessa' (Ceusters *et al*., 2019) was also used to identify experimentally observed minimum and maximum metabolite accumulation levels for the day and night-time 12-h periods and this information was used to constrain lower and upper bounds on the respective linker fluxes. The original data used for calculating these lower and upper bounds, including the necessary unit conversion steps, is available in Tables S2 and S3. Such constraints on metabolite flux accumulations assisted the model to avoid flux distributions with unrealistically high metabolite accumulations (Töpfer *et al*., 2020) and resulted in metabolite accumulation and remobilization trends in-line with the experimental data from CAM leaves (Fig. S3). Note that the amounts of these metabolites that accumulated in the model were not fixed, just constrained within lower and upper bounds and as such their accumulation rates remain a model prediction and matched well to the experimental data. As such we demonstrate the utility of the diel FBA approach further used in this study, to model realistic metabolic behavior.

Finally, fluxes representing the export of sucrose and a range of amino acids to the phloem (phloem export reaction) during the different temporal phases were constrained such that

the day-time phloem export fluxes were three-fold higher than the night-time fluxes in accordance with data reported in *Arabidopsis* (Brauner *et al*., 2018) and as applied in previous CAM models (Cheung *et al*., 2014; Shameer *et al*., 2018). This was achieved by introducing a metabolite "Phloem_e*n*" (where *n* in the metabolite ID depends on the temporal phase) as the product of the phloem export reaction in each temporal phase and creating a sink reaction (with ID "Diel_phloem_export") that consumes the newly introduced "Phloem_e*n*" metabolites with a stoichiometry of 0.75 or 0.25 depending on whether the temporal phase the metabolite belongs to day- or night-time respectively. It should be noted that information on the composition of phloem sap from *Phalaenopsis* is not available in literature. Hence, given the fact that small changes in metabolite stoichiometry of the reaction representing the objective of the system has been shown to only have negligible impact on flux through primary metabolism (Yuan *et al*., 2016), the phloem sap composition of PlantCoreMetabolism v2.0 (which is based on data from *Solanum lycopersicum*) was used in this study.

Model refinements

To further refine the metabolic model for a ME-type CAM leaf, three particular constraints were added. Firstly, PEPCK was turned off to force the model to use ME as the decarboxylating enzyme. Secondly, flux through cytosolic/plastidic NADP-malic enzyme (ME) was constrained to be eight times lower as flux through mitochondrial NAD-ME based on temporal enzyme activity measurements (see Fig. S4 and Methods S1) in *Phalaenopsis* 'Edessa' and *Kalanchoë fedtschenkoi* (both starch-storing, ME-type) and data published in Dever *et al*. (2015). Thirdly, flux through plastidic pyruvate orthophosphate dikinase (pPPDK) was constrained to be twice as low as flux through cytosolic PPDK (cPPDK) based on evidence in *K. fedtschenkoi* (Kondo *et al*., 2000).

In PlantCoreMetabolism v2.0, pyruvate translocation between the cytosol and mitochondria is facilitated by a reversible mitochondrial pyruvate carrier (MPC). However, a recent study by Le *et al*. (2021) demonstrated that the MPC acts only as a mitochondrial pyruvate importer. Hence the MPC in all 12 temporal phases of the model was allowed to facilitate only the import of pyruvate into mitochondria and a new pyruvate channel was added to the model to facilitate the export of mitochondrial pyruvate to the cytosol. Different

mitochondrial pyruvate export mechanisms (i.e. pyruvate/H^+ symport, pyruvate/H^+ antiport, and a pyruvate channel) have been explored *in silico*.

Scripts to generate the 12-phase CAM model from the Shameer *et al*. (2022) model are available on GitHub (https://github.com/stijndaems/Daems_et_al_CAM_2024). An illustration of key steps in the development of the 12-phase ME-CAM model and model constraints is presented in Fig. 1. A list of all constraints applied on the model is available in Table S4.

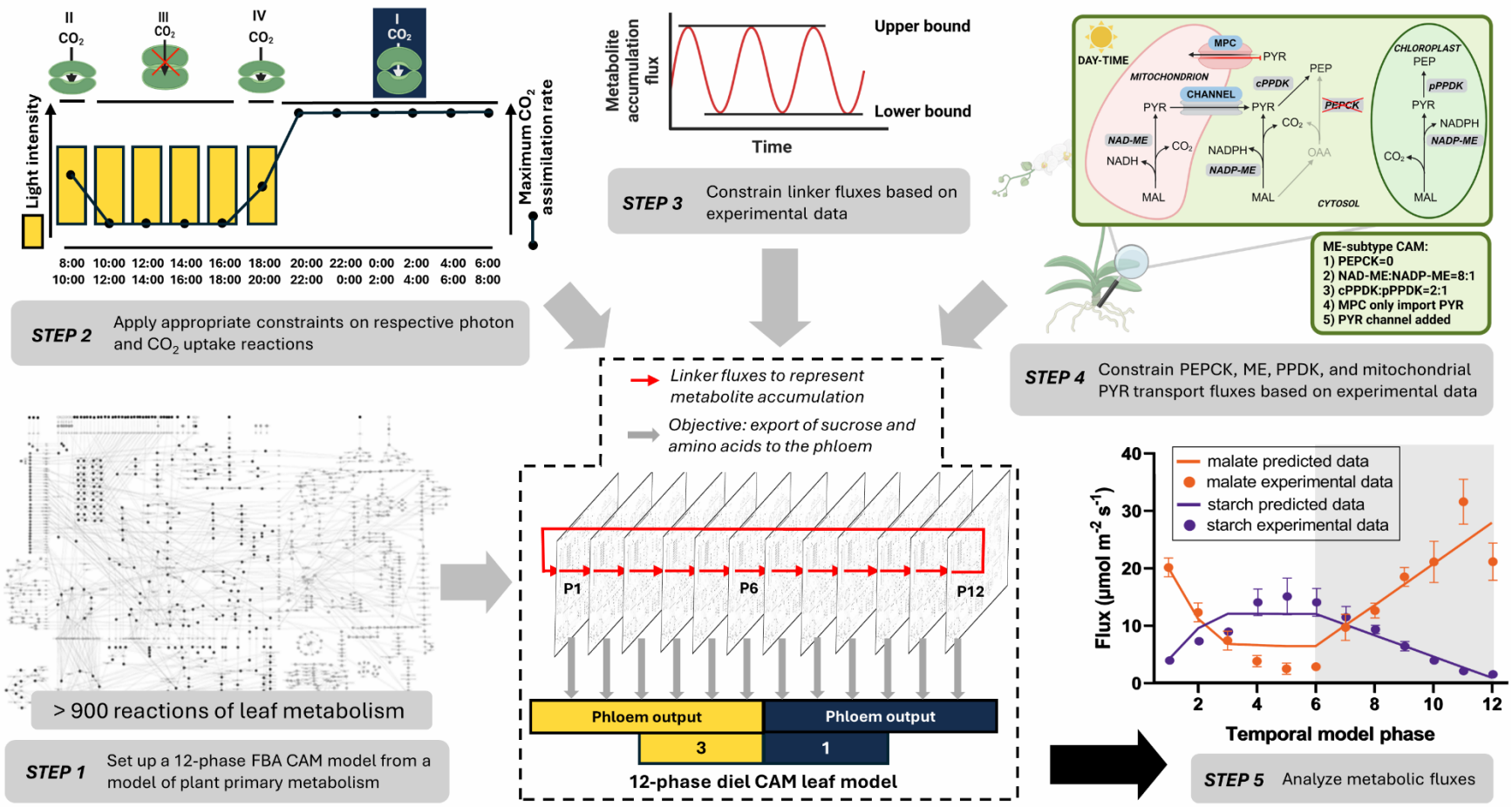

Figure 1. Overview of the different model-construction steps to develop a 12-phase malic enzyme (ME)-type CAM modelling framework. A 12-phase (2-h time resolution) leaf model was constructed by concatenating copies of a core model of plant primary metabolism (Shameer *et al.*, 2022). The individual models were connected via linker reactions that allowed the transfer of storage compounds in the vacuole and the plastid between successive models. The day:night ratio of phloem output was set to 3:1 based on previous estimates (Cheung *et al.*, 2014) (Step 1). P1 and P6 refer to the first and final temporal model phases of the light period, respectively, whereas P12 refers to the final temporal model phase of the night. Light uptake was constrained by the diel light curve. The four CAM phases of gas exchange were integrated in the model by constraining CO_2 exchange between the leaf and the

environment (Step 2). Lower and upper bounds were placed on the quantity of carboxylic acids (malate, citrate, and isocitrate), sugars (glucose, fructose, and sucrose), and starch that were allowed to accumulate in the vacuole or plastid (for starch) based on previously-published experimental metabolite data (also in a 2-h time resolution) from the starch-storing, ME-type CAM orchid, *Phalaenopsis* 'Edessa' (Ceusters *et al*., 2019) (Step 3). To further refine the metabolic model for a ME-type CAM leaf, we constrained PEPCK to carry zero flux, a flux ratio of NAD-ME:NADP-ME to 8:1, and cPPDK:pPPDK to 2:1. As the mitochondrial pyruvate carrier (MPC) acts only as a mitochondrial pyruvate importer (Le *et al*., 2021), we forced MPC to only allow pyruvate import and included a pyruvate channel mechanism to the model to re-allow export of mitochondrial pyruvate (Step 4). The model predicted metabolite accumulation and remobilization trends for malate and starch in-line with the experimental data from CAM leaves (Step 5).

Flux balance analysis (FBA) and flux variability analysis (FVA)

Flux balance analysis (FBA) (Orth *et al*., 2010) is a modelling approach popularly used to study steady-state metabolic fluxes in a wide range of biological systems. In this study, steady-state diel metabolism of a CAM leaf was modelled using parsimonious FBA (pFBA) (Lewis *et al*., 2012) with the export of sucrose and amino acids into the phloem (ID "Diel_phloem_export") as the objective function, using the COBRApy package version 0.22.1 (Ebrahim *et al*., 2013). pFBA is an extension of FBA that in addition to maximization of the objective, also minimizes the total flux in the system (Lewis *et al*., 2012).

Flux Variability Analysis (FVA) is an extension of FBA. FBA returns only one flux distribution, however, alternative solutions with the same value for the objective function may exist. FVA can be used to determine the range of feasible fluxes through one or more metabolic reactions consistent with a maximum through the objective function (Mahadevan & Schilling, 2003). In this study, FVA was used to determine the range of flux values through major CAM and proton-involved reactions using the FVA function implemented in COBRApy version 0.22.1.

Mitochondrial NAD-malic enzyme (ME) and cytosolic/plastidic NADP-ME assays

Experimental determinations of temporal ME activities in *Phalaenopsis* 'Edessa' and *Kalanchoë fedtschenkoi*, to assist the process of model refinement, were performed according to Dever *et al*. (2015) with modifications as described in Methods S1.

Results

Intracellular proton fluxes in a malic enzyme-type CAM leaf during the light period

Both the temporal (i.e. 2-h time interval, 12 model phases) and spatial resolution (i.e. proton fluxes inside the different organelles) were depicted to gain more insights into the diel kinetics of proton fluxes in a CAM mesophyll cell. Fig. 2 shows flux maps of the major reactions that produce or consume protons during day-time in the 12-phase ME-type CAM model. In the cytosol, as expected, massive import of protons was predicted in the temporal model phases representing the first half of the day (P1-P2-P3) concomitant with transport of malate out of the

vacuole (Fig. 2). Cytosolic protons were mainly imported into the mitochondrion via the mitochondrial phosphate carrier (PiC, Pi/H^+ symport) that co-imported Pi as required for ATP biosynthesis. This process was active during the whole light period, but was especially strongly operating during the first half of the day, which matched the kinetics of vacuolar malate and proton efflux to the cytosol. A table of diurnal proton fluxes through PiC and vacuolar malate efflux is presented in Table S5. Most (ca. 95%) of the mitochondrial protons were involved in the respiratory electron transport chain (mETC) (oxidative phosphorylation, see specific flux values in all temporal model phases for NADH dehydrogenase (Complex I), cytochrome *c* reductase (Complex III) and cytochrome *c* oxidase (Complex IV) in Table S6) to establish a proton gradient which drives the ATP synthase complex for the generation of ATP (see specific flux value for mitochondrial ATP synthase (Complex V) in Table S6). Model predictions showed that the majority (>75%) of this mitochondrial-generated ATP (19.85 μmol m^{-2} s^{-1} in P2) was exported towards the cytosol to meet the high energy demand of day-time gluconeogenesis. Note that, in each temporal model phase, a substantial proportion (>30%) of mitochondrial protons was consumed in the matrix to reduce molecular oxygen to water (at Complex IV, cytochrome *c* oxidase) and synthesize ATP (i.e. an OH^- group is released from Pi when it binds to ADP, which subsequently binds to H^+ in the matrix to form water). As such protons did not show net accumulation inside the mitochondrion. In addition, the modelling framework did not predict any activity of the tricarboxylic acid (TCA) cycle during these diurnal model phases (Fig. 2) (see specific flux values for citrate synthase in Table S6). The oxidative decarboxylation of malate by mitochondrial NAD-ME provided reducing equivalents (NADH), which served as an electron donor to the mETC.

As a consequence of the activity of the plastidic malate valve, i.e. plastidic malate dehydrogenase (pMDH) converting oxaloacetate (OAA) to malate and cytosolic MDH (cMDH) operating in the opposite direction, plastidic protons were shuttled from the chloroplast to the cytosol. cMDH released these protons concomitant with reducing equivalents (NADH) inside the cytosol at the rate of 7.87 μmol m^{-2} s^{-1} in P2. Specific flux values in all temporal model phases for pNADP-MDH, plastidic malate/OAA translocator, and cNAD-MDH are presented in Table S6. About 65% of plastidial protons was involved in the pETC (photophosphorylation) where protons were translocated across the thylakoid membrane (at the rate of 109.31 μmol m^{-2} s^{-1} in P2). The resulting proton gradient was used to energize the ATP synthase complex. In contrast to

the mitochondrion, the chloroplast played no role in supplying ATP to the cytosol, but provided the ATP required for running the CBB cycle and the generation of ADP-glucose (precursor for starch). In addition, a significant amount of protons was consumed in the stroma by ferredoxin-$NADP^+$ reductase (FNR) (at the rate of 24.20 μmol m^{-2} s^{-1} in P2) for the generation of NADPH required primarily also to support the CBB cycle.

The amount of protons in the vacuole was maximal at dawn (model phase P1) (see specific flux value for 'PROTON_v12_accumulation' in Table S6). During the first half of the photoperiod protons were exported at high rates towards the cytosol concomitant with malate to reach near zero levels around dusk (model phase P6) (see specific flux value for 'PROTON_v5_accumulation' in Table S6). Note that proton fluxes in general, relative to the cytosol as well as in the organelles, dramatically declined during the second half of the photoperiod when malate decarboxylation rates were low, indicating that proton balancing in CAM might especially be challenging during the first half of day-time.

Analysis of night-time metabolism to ensure our modelling framework was performing typical CAM behavior during the dark (P7-P12) was also performed. Flux maps and description of the major proton-producing and -consuming reactions during night-time in the 12-phase ME-CAM model are included in Fig. S5 and Notes S1.

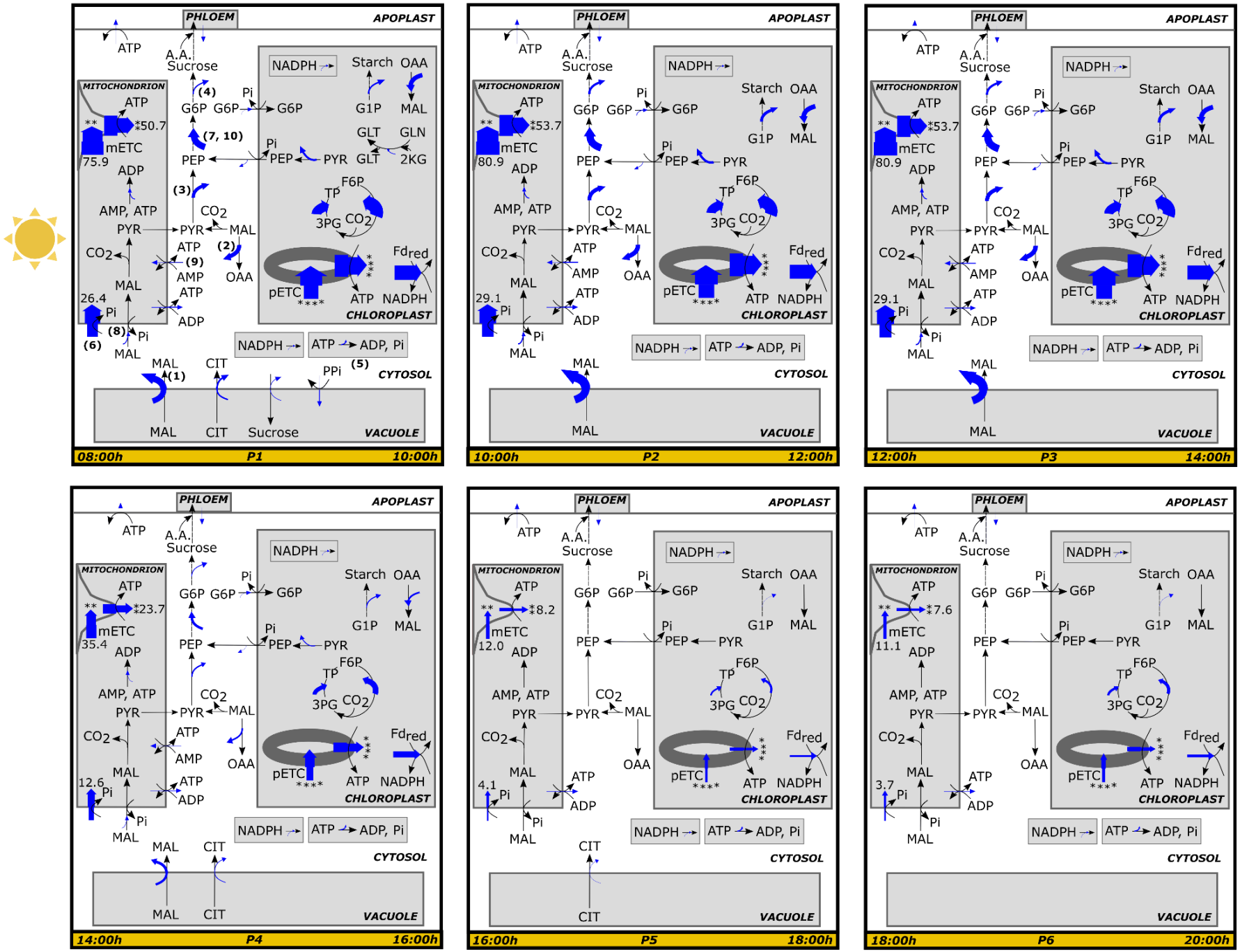
PHLOEM
APOPLAST
ATP
A.A.
Sucrose
NADPH
Starch
OAA
MITOCHONDRION
G1P
MAL
GLT
GLN
2KG
mETC
PEP
PYR
F6P
TP
3PG
CO2
pETC
Fdred
ADP
AMP, ATP
MAL
OAA
NADPH
CHLOROPLAST
CYTOSOL
VACUOLE
CIT
PPi
Sucrose
08:00h
P1
10:00h
10:00h
P2
12:00h
12:00h
P3
14:00h
14:00h
P4
16:00h
16:00h
P5
18:00h
18:00h
P6
10 µmol m-2 s-1

Figure 2. Flux maps representing major diurnal (P1-P6) proton-producing and proton-consuming reactions in the 12-phase malic enzyme-CAM model. Photon uptake in CAM was constrained to 100 μmol m^{-2} s^{-1} during day-time and parsimonious optimization was applied to compute the flux distribution that maximized the amount of sucrose and amino acids exported to the phloem. All reactions producing and consuming protons with a proton flux greater than 0.5 μmol m^{-2} s^{-1} were included in the flux maps. Blue arrows represent proton fluxes and their thicknesses are scaled to the proton flux value (as μmol H^+ m^{-2} s^{-1}, scale is shown in the box at the bottom center). Notice that proton flux through the mitochondrial electron transport chain (mETC) is twice as large as depicted by the thickness of the blue arrow (notice two asterisks). Proton flux through the plastidic electron transport chain (pETC) is four times as large as depicted by the thickness of the blue arrow (notice four asterisks). Numbers inside mitochondria indicate the number of protons involved in that reaction (as μmol H^+ m^{-2} s^{-1}). Solid black lines highlight one particular transport or conversion reaction, while dashed black lines represent a series of sequential reactions. Boxes inside the cytosol and chloroplast depict reactions used to represent non-growth-associated maintenance. Numbers inside brackets on the flux map of P1 from 1 to 5 represent the five most significant cytosolic proton-producing reactions and from 6 to 10 the five most significant cytosolic proton-consuming reactions (also see Fig. 3). Abbreviations are: 2KG, 2-ketoglutarate; 3PG, 3-phosphoglycerate; A.A., amino acids; ADP, adenosine diphosphate; AMP, adenosine monophosphate; ATP, adenosine triphosphate; CIT, citrate; F6P, fructose 6-phosphate; Fd_{red}, reduced ferredoxin; G1P, glucose 1-phosphate; G6P, glucose 6-phosphate; GLN, glutamine; GLT, glutamate; MAL, malate; mETC, mitochondrial electron transport chain; OAA, oxaloacetate; PEP, phospho*enol*pyruvate; Pi, inorganic phosphate; pETC, plastidial electron transport chain; PYR, pyruvate; TP, glyceraldehyde 3-phosphate.

Major cytosolic proton-producing and proton-consuming reactions in a ME-type CAM mesophyll cell during the light period

Quantitative comparisons were made among all reactions producing and consuming cytosolic protons during day-time (Fig. 3). Vacuolar malate efflux accounted for one third (34%) of the total amount of protons produced in the cytosol. Cytosolic malate dehydrogenase (cMDH), working as part of the malate valve, was also observed to produce a significant amount of protons inside the cytosol (19% of the total proton-producing flux). Cytosolic pyruvate orthophosphate dikinase (cPPDK), which catalyzes the conversion of pyruvate to phospho*enol*pyruvate (PEP), also carried a large proton-producing flux (16% of the total proton-producing flux). Cytosolic soluble pyrophosphatase (sPPase), which catalyzes the hydrolysis of inorganic pyrophosphate to generate orthophosphate, and non-growth-associated maintenance (NGAM, a proxy for all ATP costs associated with maintenance) were each responsible for about 10% of total cytosolic proton production.

More than half (53%) of all cytosolic protons were transported to the mitochondrion by the mitochondrial Pi/H^+ symporter (PiC). Glyceraldehyde 3-phosphate dehydrogenase (GAPDH), a key enzyme in day-time gluconeogenesis for the conversion of 1,3-

bisphosphoglycerate (DPG) to glyceraldehyde 3-phosphate (TP), accounted for about 25% of the total proton-consuming flux. Import of cytosolic malate into the mitochondrion by the dicarboxylate transporter (DIC, malate/Pi antiport), the mitochondrial ATP/AMP carrier (mADNT1), and phosphoglycerate kinase (cPGK) only represented ca. 10% of the total cytosolic proton-consuming flux. A similar analysis of the major cytosolic proton-producing and -consuming fluxes during night-time for the ME-type model is presented in Fig. S6 and Notes S2. The complete set of cytosolic proton-producing and proton-consuming reactions during both day and night, sorted according to their proton flux values (flux values are the sum of 6 model phases) and relative contribution, is available in Tables S7 and S8.

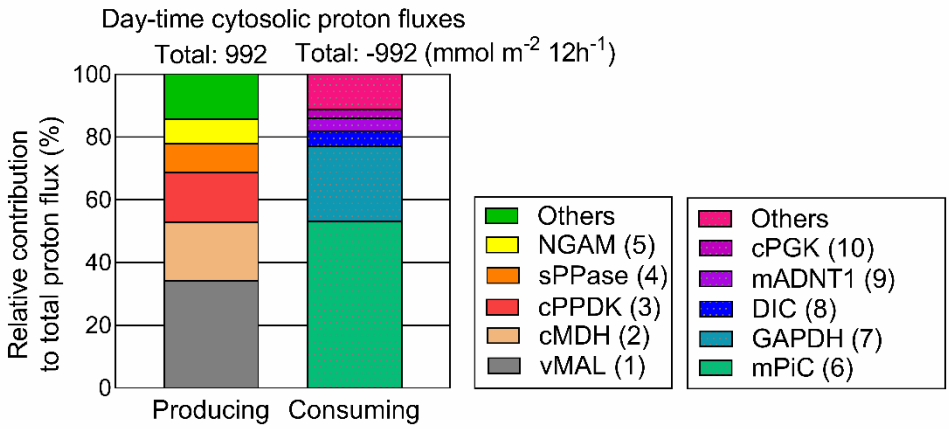

Figure 3. Key cytosolic proton-producing and proton-consuming reactions during day-time in a malic enzyme-type CAM mesophyll cell. Diel FBA was used to model leaf metabolic flux distributions in ME-CAM leaves grown under 100 µmol m^{-2} s^{-1} photosynthetically active radiation (PAR). The stacked bar chart depicts the contribution of the five most significant cytosolic proton-producing and -consuming reactions during day-time as a percentage to the total amount of protons produced or consumed. This total amount is shown above each bar (fluxes are the sum of six separate diurnal model phases, P1-P6, in mmol m^{-2} $12h^{-1}$). Numbers inside brackets from 1 to 5 represent the five most significant cytosolic proton-producing reactions (sorted from most to least significant), while 6 to 10 represent the five most significant cytosolic proton-consuming reactions (again sorted from most to least significant). These numbers correspond to the numbers shown on Fig. 2 for model phase 1 (P1). vMAL, vacuolar malate efflux; cMDH, cytosolic malate dehydrogenase; cPPDK, cytosolic pyruvate orthophosphate dikinase; sPPase, cytosolic soluble pyrophosphatase; NGAM, non-growth-associated maintenance; mPiC, mitochondrial P_i/H^+ symporter; GAPDH, glyceraldehyde 3-phosphate dehydrogenase; DIC, dicarboxylate transporter (malate/P_i antiport); mADNT1, mitochondrial ATP/AMP carrier; cPGK, cytosolic phosphoglycerate kinase.

The mitochondrial PiC transporter is key to secure diurnal cytosolic proton homeostasis

Since the mitochondrial Pi/H^+ symporter (PiC) emerged as the key actor to relieve the cytosol of its diurnal proton pressure, we elaborated on its possible importance by inhibiting

PiC in the model and studying the resulting flux distribution (Fig. 4a, b). Diel phloem export flux was reduced by more than 20% when PiC activity was inhibited, indicating a consistently lower productivity (Fig. 4b). In this PiC inactive scenario, a large amount of malate (18.08 μmol m^{-2} s^{-1} in P2) was synthesized in the mitochondrion via mMDH using oxaloacetate. Mitochondrial Pi was mainly delivered via the mitochondrial dicarboxylate carrier (DIC), primarily in exchange for malate. Malate was thus partly exported to the cytosol instead of being decarboxylated (which should be typical for CAM). Flux analysis in this inactive PiC configuration also revealed that pyruvate was imported into the mitochondrion via the mitochondrial pyruvate carrier (MPC) to facilitate proton uptake. This pyruvate was then exported back towards the cytosol along with NAD-ME-generated pyruvate. This is in contradiction to the finding of Le *et al.* (2022) that two distinct pyruvate pools exist in plant mitochondria, and that pyruvate imported from the cytosol (via the MPC) should be designated for the tricarboxylic acid (TCA) cycle whilst pyruvate generated by NAD-ME should be exported towards the cytosol. Specific flux values of all reactions in this alternative model are presented in Table S6. From all these considerations we suggest that PiC is indeed optimal to supply Pi and protons to the mitochondrion to drive mitochondrial ATP synthase and to secure cytosolic proton homeostasis during diurnal CAM simultaneously.

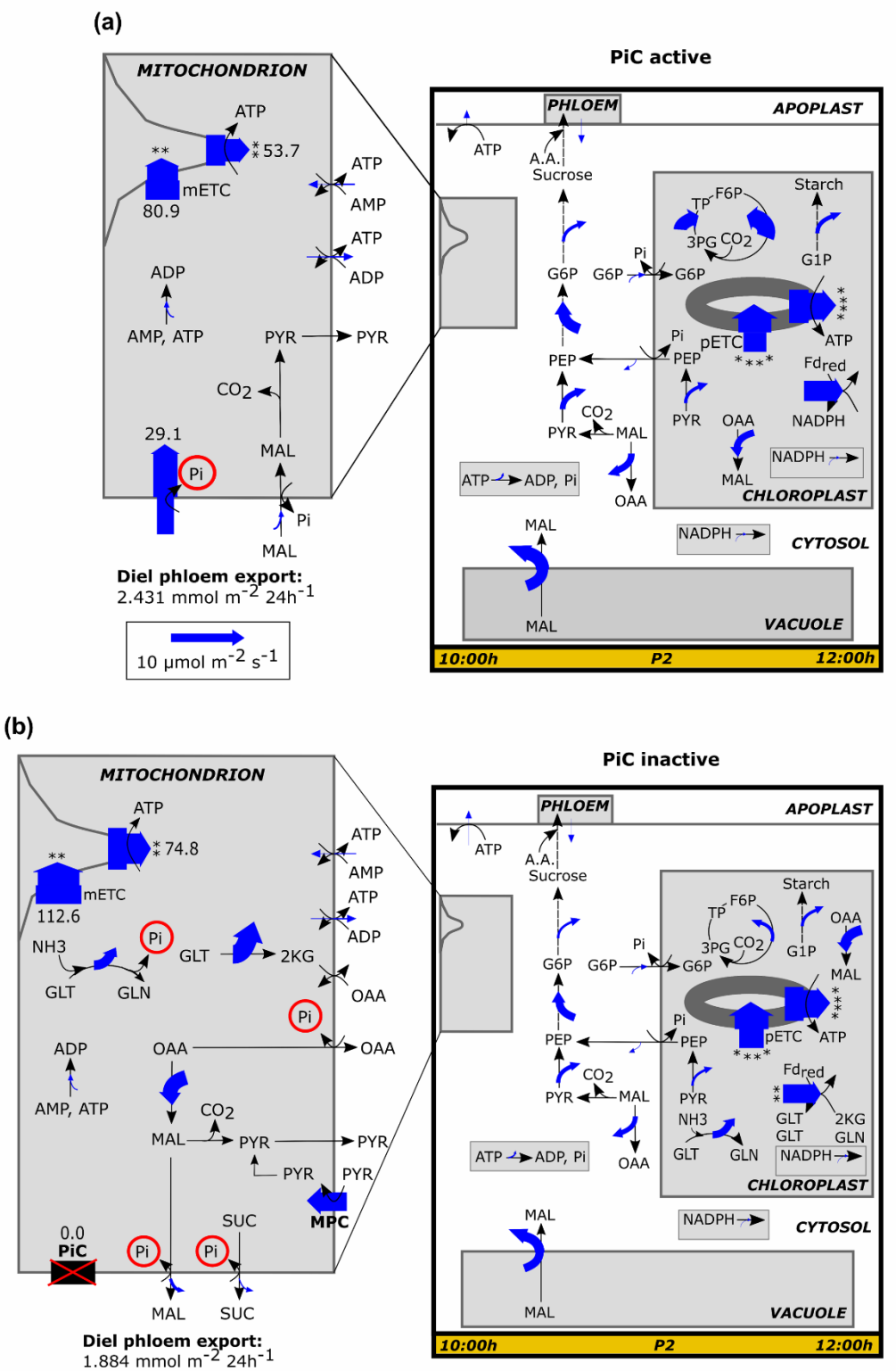

Figure 4. Schematic representation of the proton flux distribution when PiC is active or turned off. Flux maps of temporal model phase 2 (i.e. P2, when malate decarboxylation rate is relatively high) representing proton-producing and proton-consuming reactions that occurred in the initial (a) and forced model when PiC activity is inhibited (b). Red circles indicate sources of Pi. Abbreviations are as for Fig. 2, as well as: MPC, mitochondrial pyruvate carrier; SUC, succinate.

Metabolic modelling identifies a pyruvate channel as the most efficient mechanism for mitochondrial pyruvate export in plants

Without any constraints on pyruvate translocation between the cytosol and mitochondria, the MPC initially carried a large pyruvate/H^+ export flux (symport) to the cytosol (157 mmol m^{-2} $12h^{-1}$ during day-time) (Fig. 5a), which is in contradiction with the findings of Le *et al.* (2021). Therefore, the MPC was constrained to only allow pyruvate import. To re-allow pyruvate export, three possible mitochondrial pyruvate export mechanisms (i.e. H^+-PYR symport, H^+-PYR antiport and a PYR channel) were added separately to the model to unveil their impact on specific CAM cycle fluxes (Fig. 5b, c, d).

When a H^+-PYR symport mechanism was operating (similar as the MPC), protons were exported together with NAD-ME-derived pyruvate. To compensate for these exported protons, PiC increased its diel proton and Pi flux which also resulted in an increase in mATP synthase flux (Fig. 5b). When a H^+-PYR antiport mechanism was active, all NAD-ME-derived pyruvate was exported with concomitant mitochondrial H^+ uptake. These additional protons were re-exported towards the cytosol at the cost of reducing power (Fig. 5c). In this scenario, ca. 15% and 11% lower diurnal fluxes through PiC and mATP synthase were observed respectively compared to the symport mechanism. IDs of reactions re-exporting protons are included in Table S9. When a pyruvate channel was applied, all NAD-ME-derived pyruvate was exported to the cytosol without any proton translocation and the diurnal fluxes through PiC and mATP synthase were comparable to the antiport mechanism (Fig. 5d).

Differences in particular CAM cycle flux values among the different mitochondrial pyruvate efflux mechanisms were generally small. However, the highest flux through diel phloem export, PEPC, vacuolar malate influx and efflux, malic enzyme and PPDK was observed when a pyruvate channel was active in the model, while mATP synthase flux, and thus energy requirements were minimized simultaneously. These model predictions suggest a pyruvate channel mechanism as the most efficient for mitochondrial pyruvate export in plants.

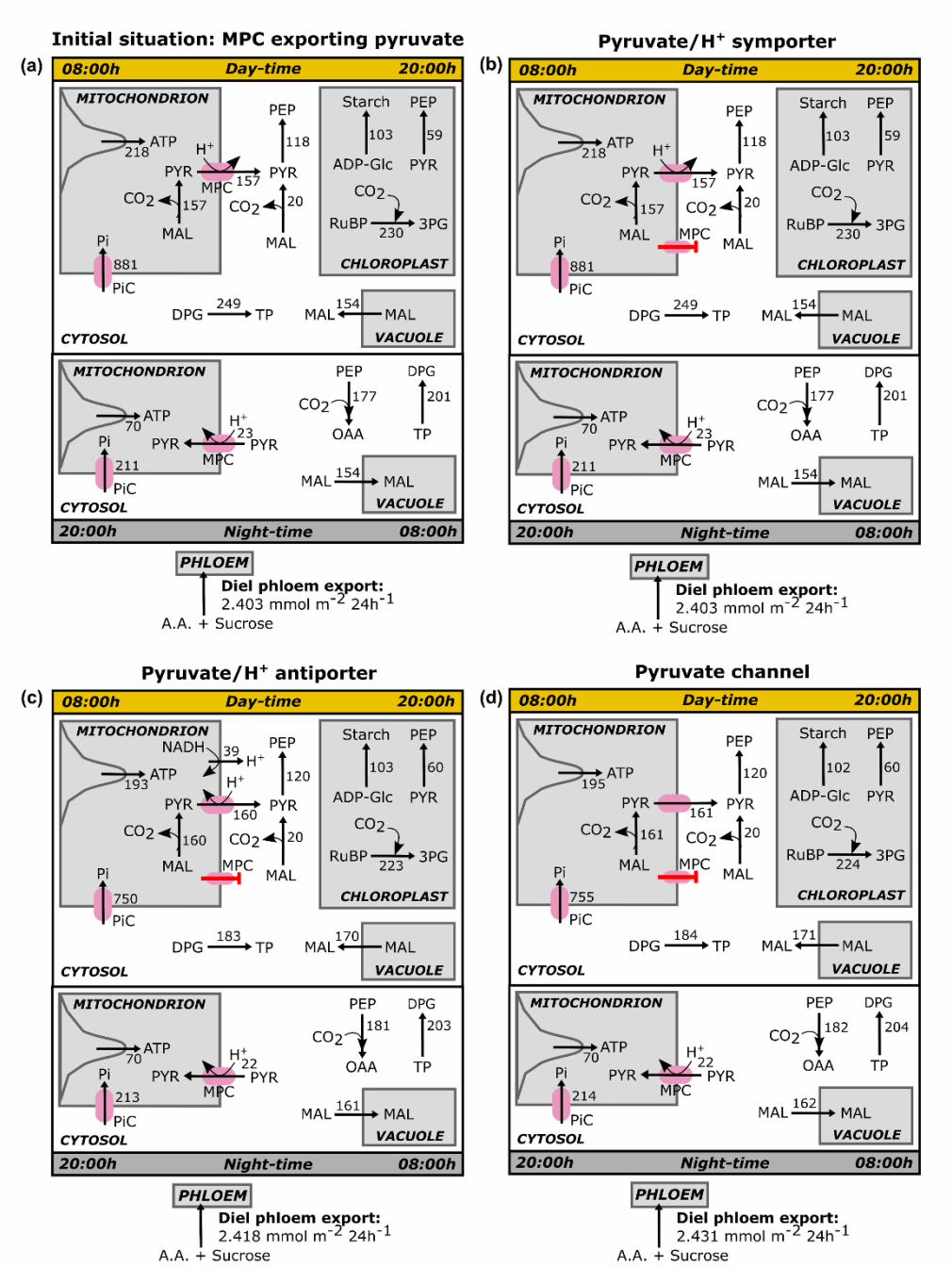

Figure 5. Flux maps depicting flux distributions under different potential mitochondrial pyruvate export mechanisms. Initial situation where pyruvate is exported via the mitochondrial pyruvate carrier (MPC) (a), pyruvate/H^+ symport (b), pyruvate/H^+ antiport (c), and a pyruvate channel (d). The MPC in plants does not work backwards to export NAD-ME-derived pyruvate (Le *et al*., 2021) as indicated by the red line in (b), (c), and (d). Differences in particular CAM cycle flux values among the different mitochondrial pyruvate efflux mechanisms were generally small. Therefore, arrow thickness is not scaled to the flux value, but numbers on the flux maps in the proximity of the arrows represent the exact flux through the reaction. Units of flux were converted from µmol m^{-2} s^{-1} to mmol m^{-2} $12h^{-1}$ to depict summarized flux values over all diurnal (P1-P6) and nocturnal (P7-P12) temporal model phases. Abbreviations are as for Fig. 2 as well as MPC, mitochondrial pyruvate carrier; ADP-Glc, ADP-glucose; RuBP, ribulose 1,5-bisphosphate; DPG, 1,3-bisphosphoglycerate.

The significance of PiC and GAPDH in cytosolic proton homeostasis is robust to changes in modelling parameters

To examine whether flux predictions of key diurnal cytosolic proton-consuming reactions (PiC and GAPDH) were sensitive to parameters used in the model (which also vary among CAM species), the impact of changes in (a) Rubisco carboxylase/oxygenase (V_c/V_o) ratios, (b) non-growth associated maintenance cost, (c) NAD-ME:NADP-ME flux ratio, (d) cPPDK:pPPDK flux ratio, (e) the decarboxylation mechanism (from ME to PEPCK), (f) type of leaf storage carbohydrate, and (g) (iso)citrate accumulation were studied. Generally, PiC and GAPDH consistently retained their significant contribution to cytosolic proton consumption by collectively consuming between 68% and 79% of all cytosolic protons during day-time across the wide range of tested scenarios (Table S19). Results are presented and described in more detail for each scenario in Tables S10-S18 and Notes S5. A description of the major differences between a ME- and PEPCK-type decarboxylation pathway as well as analyses of key cytosolic proton reactions in the PEPCK model are shown in Figs S7, S8, Tables S14, S15, and Notes S3, S4.

In addition, FVA was performed to identify the range of feasible values for the vacuolar proton remobilization, PiC and GAPDH fluxes (see Methods). Flux variability range of these fluxes showed to be negligible as the minimum and maximum were almost the same as the predicted flux. Hence, this strengthens the capability of drawing model-based conclusions of CAM proton homeostasis. A list of reaction names and their predicted flux variability ranges for this model are shown in Table S20.

Discussion

The 12-phase CAM model (Fig. 1) allowed us to study the complex metabolic process of pH homeostasis in a systematic way by identifying and quantifying intracellular proton-producing and proton-consuming reactions (Figs 2, 3). Our analysis especially focused on the diurnal process of CAM, leading to four main findings which are discussed in more detail below and summarized in Fig. 6. Throughout the development of this FBA model, several species-specific assumptions were made but these did not alter the main conclusions. Our findings consistently demonstrate the significant role for PiC and GAPDH in cytosolic proton homeostasis across the wide range of tested, species-specific, modelling parameters (i.e. collectively consume between 68% and 79% of all cytosolic protons during day-time across

all scenarios) (Table S19). By identifying two key molecular targets (mitochondrial PiCs and cytosolic GAPDH) associated with biochemical reactions controlling CAM cytosolic proton homeostasis during day-time, we also inform experimental genetic and/or pharmacological manipulation approaches to further uncover their importance in CAM empirically.

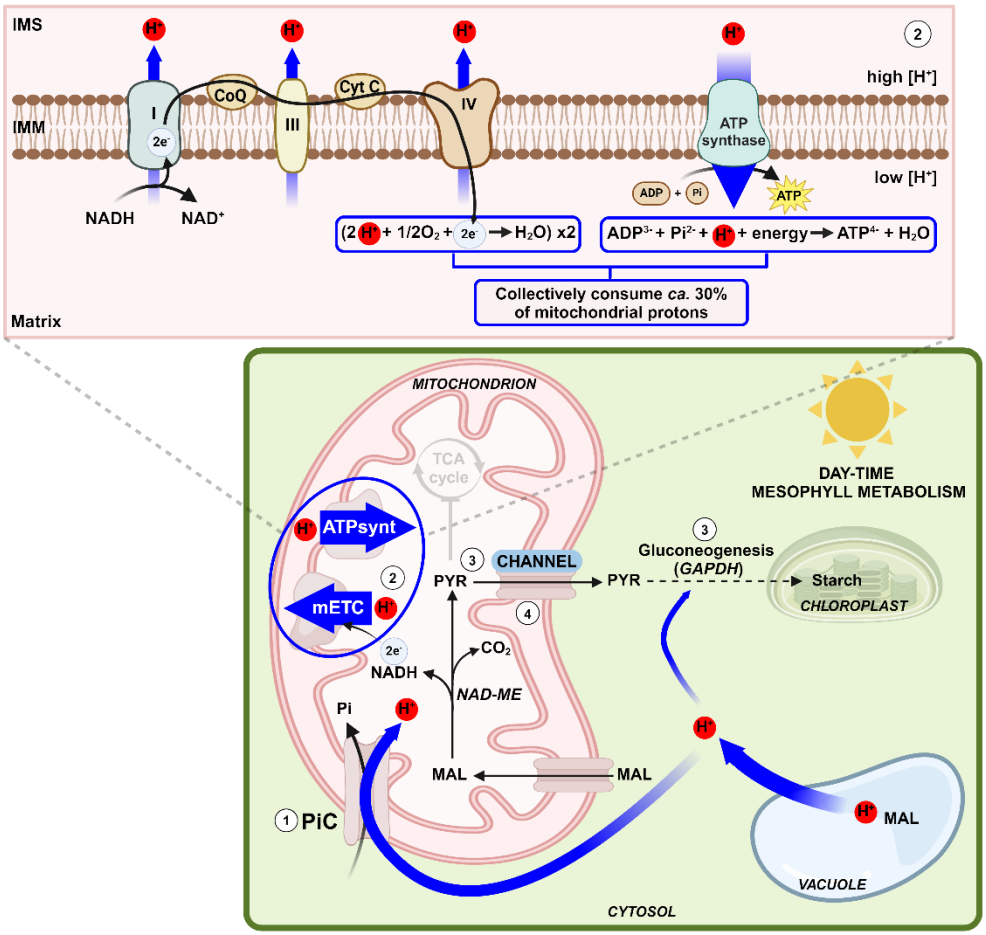

Figure 6. Schematic representation of key metabolic steps to secure diurnal proton homeostasis in a malic enzyme-type CAM mesophyll cell. The mitochondrion is enlarged to depict envisaged key steps in proton homeostasis. Proton fluxes are depicted as blue arrows, while reactions that are not proton-linked are depicted by black arrows. Red dots represent protons. Diurnal vacuolar malate efflux releases a substantial amount of protons inside the cytosol. These protons are mainly consumed by mitochondrial phosphate carriers (PiCs) that provide Pi and protons (in co-transport) to the mitochondrial matrix to sustain oxidative phosphorylation (1). The oxidative decarboxylation of malate by mitochondrial NAD-ME produces reducing equivalents (NADH), which are required to supply electrons to the mitochondrial electron transport chain (mETC). Electrons passing through the mETC causes protons to be pumped from the matrix towards the intermembrane space (IMS), thereby creating a proton gradient across the inner mitochondrial membrane (IMM). This proton gradient is subsequently used by the ATP synthase complex to generate ATP, using ADP and Pi, in order to meet the high energy demand during CAM Phase III. Note that protons in the mitochondrial matrix are consumed (*ca.* 30% of the total amount of mitochondrial protons) during the reduction of molecular oxygen to water, catalyzed by

cytochrome *c* oxidase (COX, Complex IV), at the end of the mETC. Also, during the conversion of ADP to ATP, an OH^- group is released from Pi, subsequently binding to H^+ in the matrix to form water. As such, a continuous supply of protons to the matrix via the PiC is important to sustain oxidative phosphorylation. Equations of these mitochondrial proton-consuming reactions are given in the detailed schematic of the mETC (2). The model predicted that NAD-ME-derived pyruvate is exclusively exported towards the cytosol and quantitively converted to the level of storage carbohydrate via gluconeogenesis rather than being oxidized in the TCA cycle (3). Model predictions did not show any diurnal TCA cycle activity and as such no $FADH_2$ molecules are formed. Therefore, succinate dehydrogenase (Complex II) is not depicted in the mETC on the figure. Model predictions indicate glyceraldehyde 3-phosphate dehydrogenase (GAPDH) as a key metabolic point that also consumes a substantial amount of cytosolic protons during day-time gluconeogenesis (3). GAPDH catalyzes the conversion of 1,3-bisphosphoglycerate to glyceraldehyde 3-phosphate, thereby consuming protons and reducing power (NADH). *In silico* analysis suggests that diurnal mitochondrial pyruvate export in ME-type CAM plants is most efficient via a channel mechanism (4). Abbreviations are: CoQ, coenzyme Q; Cyt *C*, cytochrome *c*; GAPDH, glyceraldehyde 3-phosphate dehydrogenase; IMM, inner mitochondrial membrane; IMS, intermembrane space; MAL, malate; mETC, mitochondrial electron transport chain; NAD-ME, mitochondrial malic enzyme; PiC, mitochondrial Pi/H^+ symporter; PYR, pyruvate; TCA, tricarboxylic acid cycle.

Mitochondrial PiCs as main diurnal cytosolic proton balancers (1-2)

The modelling work shows that >50% of the cytosolic protons were consumed by the mitochondrial phosphate carrier (PiC) during day-time (Fig. 3). Its proton-consuming flux was particularly high during the first half of the photoperiod concomitant with high rates of vacuolar malate efflux and processing (high tonoplast transmembrane gradient; Fig. 2), which is consistent with experimental data of declining diurnal malate content and titratable acidity in leaves of different CAM species (Ceusters *et al*., 2008, 2014, 2019; Abraham *et al*., 2020). In addition, unusual CAM cycle fluxes were noticed and diel phloem export diminished by more than 20% when PiC was inhibited in the model (Fig. 4b). Hence, we postulate that PiCs are key to metabolically achieve diurnal proton homeostasis in the cytosol of CAM leaf cells. PiCs are located in the inner mitochondrial membrane (IMM) and manage the uptake of phosphate (Pi) into the mitochondrial matrix, which is required for oxidative phosphorylation (Haferkamp, 2007). As PiCs catalyze a Pi/H^+ symport (Pratt *et al*., 1991) or a Pi/OH^- antiport (Stappen & Krämer, 1994), transport of Pi is coupled to the favorable inward pH gradient (matrix pH 8.1) (Shen *et al*., 2013). It is generally assumed that this pH gradient (ΔpH) across the IMM, created by the mitochondrial electron transport chain (mETC), serves as the driving force for Pi uptake (Laloi, 1999; Takabatake *et al*., 1999). At the end of the mETC (Complex IV, cytochrome *c* oxidase), protons are consumed during the reduction of O_2 to water. In addition, when ADP binds to Pi to facilitate ATP formation, an OH^- group is liberated from

Pi, subsequently binding to H^+ in the matrix to produce water (Fig. 6). As such protons do not show net accumulation inside the matrix, thereby avoiding mitochondrial acidification. Our analyses also reveal PiC as the intimate link between the consumption of cytosolic protons and their subsequent consumption by the respiratory pathway in the ME-mediated pH-stat model described by Sakano (1998), which also holds importance for C_3 and C_4 species.

Adenylate and dicarboxylate transporters in CAM mitochondria, belonging to the same mitochondrial carrier protein superfamily (mCP) as PiC, have already been identified in the common ice plant (*Mesembryanthemum crystallinum*), namely McANT2 and McDCT2 respectively (Kore-eda *et al*., 2005). Also, transcripts encoding mitochondrial dicarboxylate carrier proteins (DIC) (belonging to the same mCP superfamily as PiC), which allow import of malate in exchange for phosphate, sulphate or other dicarboxylates, were obviously more abundant after induction of CAM in different facultative species especially in the first half of the day (Cushman *et al*., 2008; Brilhaus *et al*., 2016; Ferarri *et al*., 2020). Higher transcript abundance of DIC is associated with increased rates of malate uptake into mitochondria for decarboxylation via NAD-ME. A close examination of PiC fluxes in previously-published FBA models further supports our findings. Considerable day-time flux through PiC (-29.73 $\mu mol\ m^{-2}\ s^{-1}$) was observed to supply the mitochondrion with Pi for ATP synthesis in the model from Cheung *et al*. (2014). The models by Shameer *et al*. (2018) and Tay *et al*. (2021) also showed a significant involvement of PiC in maintaining day-time cytosolic proton homeostasis by consuming about 64% and 58% of cytosolic protons respectively.

Proton delivery by PiC is essential to fuel mitochondrial metabolism in order to meet the high energy demand during CAM phase III (1-2)

Diurnal mitochondrial ATP synthesis via oxidative phosphorylation depends on the supply of substrates (ADP and Pi) and protons inside mitochondria. The continuous delivery of protons from the cytosol via the PiC is especially important since our model indicated that about one third of the mitochondrial protons gets consumed during oxidative phosphorylation. Phosphate is taken up concomitantly with protons through the PiC, whilst cytosolic ADP is exchanged with mitochondrial ATP, via an ADP/ATP carrier (AAC) (Fig. 2). AAC1 and PiC1 are considered to be the major carriers to replenish substrates for ATP synthesis, given their simultaneous expression in diverse tissues and highest abundance in the mitochondrial membrane proteome from *Arabidopsis* (Millar & Heazlewood, 2003). PiC is highly expressed in developing organs, where tissues contain actively dividing cells requiring

a high energy supply. This observation suggests that PiC, together with AACs, fulfills a major physiological function in the energy supply in plant cells (Laloi, 1999). Over-expression of PiC protein can lead to a higher ATP content compared with wild-type *A. thaliana*, indicating a possible correlation between energy states and expression levels of PiCs (Zhu *et al*., 2012; Jia *et al*., 2015).

The importance of mitochondrial metabolism, to meet the high energy demand during Phase III, has already been debated in the past and several hypotheses have been formulated. For ME-type CAM plants, Edwards *et al*. (1982) suggested that mitochondrial oxidation of some of the NAD(P)H produced in the ME reaction might fuel extra ATP production through oxidative phosphorylation. This process has been questioned as these reducing equivalents seemed essential for the activity of cytosolic GAPDH in the gluconeogenic recovery of pyruvate (Winter & Smith, 1996). However, a cytosolic shortage in reducing equivalents is very unlikely to happen since the malate-oxaloacetate shuttle (malate valve) is capable of transferring reducing power from the chloroplast to the cytosol (Scheibe, 2004). In our model, high fluxes through the malate valve were predicted, especially during the first half of the day (Table S6). Higher rates of photosynthetic electron transport during Phase III have also been reported for several CAM plants and are consistent with these views (Maxwell *et al*., 1999, de Mattos & Lüttge, 2001). In addition, increased rates of mitochondrial NADH oxidation (Complex I, resulting in higher rates of electron transfer from NADH to the mETC), increased cytochrome *c* oxidase (COX) (Complex IV) activity, and the upregulation of mitochondrial Mn-dependent superoxide dismutase (SOD), seem common responses to the induction of CAM in facultative species (Miszalski *et al*., 1998; Broetto *et al*., 2002; Peckmann *et al*., 2012), which show experimental evidence of higher mitochondrial electron transport rates, and thus also proton consumption rates, in CAM. Different flux balance models have also indicated a consistently higher diurnal ATP production in CAM mitochondria compared to C_3. The C_3 and CAM metabolic modelling framework by Cheung *et al*. (2014) suggested that diurnal mitochondrial ATP synthase contributed for 34% of total ATP production in CAM, compared to only 18% in C_3. More recently, a comparative analysis of the energetics of C_3 metabolism and CAM also predicted that mitochondrial ATP synthase accounted for ca. 30% of total day-time ATP synthesis in CAM, in contrast to 0% in C_3 plants (Shameer *et al*., 2018).

NAD-ME-derived pyruvate is exported to the cytosol to fuel gluconeogenesis in ME-type CAM plants and contributes to day-time cytosolic proton homeostasis simultaneously (3-4)

The metabolite flux distributions observed in our CAM metabolic modelling framework did not predict any TCA cycle activity during the light period (no oxidation of pyruvate) (Fig. 2, Table S6). It has also been shown that pyruvate dehydrogenase complex (PDC) activity, which regulates the entry of pyruvate into the TCA cycle, is considerably reduced in Phase III compared to Phase I (Smith & Bryce, 1992). Comparative calculations with and without any pyruvate oxidation show that the net energy costs of Phase III metabolism can indeed be minimized if the 3-C residue from malate decarboxylation is quantitively recovered via gluconeogenesis (Winter & Smith, 1996). Moreover, experimental observations of TCA cycle activity mainly report high mitochondrial fluxes of carbon and electron transport in CAM at night (Osmond *et al*., 1988; Abraham *et al*., 2016). Le *et al*. (2022) have also demonstrated that PDC and TCA cycle enzymes in plant mitochondria exhibit a preference for utilizing imported pyruvate (via MPC) rather than NAD-ME-generated pyruvate. These findings corroborate our model predictions depicting the non-mitochondrial usage of pyruvate derived from NAD-ME and the absence of diurnal TCA cycle activity in CAM mitochondria (Fig. 2, Table S6).

Due to its inactivity during the day, the TCA cycle does not supply reducing power (NADH and $FADH_2$) to the mETC. However, the oxidative decarboxylation of malate by NAD-ME also yields reducing equivalents (NADH) inside the mitochondrial matrix (MM) in order to fuel the electron transport chain (Edwards *et al*., 1982) and establish a proton gradient to drive ATP synthase. Evidence is indeed accumulating that mitochondrial NAD-ME assisted malate decarboxylation is far more important in CAM species than its cytosolic/chloroplastic NADP-ME counterpart (Dever *et al*., 2015; Winter & Smith, 2022; Fig. S4).

In addition to its essential role in carbohydrate metabolism, gluconeogenesis seems also important for cytosolic proton homeostasis during day-time in both ME- and PEPCK-type CAM leaves (Figs 2, 3, S8A). Especially glyceraldehyde 3-phosphate dehydrogenase (GAPDH) acted as an important consumer of cytosolic protons (ca. 24% of the total amount of cytosolic protons) (Fig. 3). Increased transcript abundances of several genes encoding cytosolic glycolytic/gluconeogenic enzymes (GAPDH included) have been reported

following the salinity- or drought-induced transition from C_3 or C_4 photosynthesis to CAM in different facultative CAM species (Ostrem *et al*., 1990; Cushman *et al*., 2008; Brilhaus *et al*., 2016; Ferrari *et al*., 2020). Moreover, extractable activities of these glycolytic/gluconeogenic enzymes (GAPDH included) have been reported to increase after the induction of CAM in the inducible common ice plant (*M. crystallinum*) (Holtum & Winter, 1982; Winter *et al*., 1982). These experimental observations confirm a major participation of these glycolytic/gluconeogenic enzymes in CAM and corroborate our suggestion that maintaining an unperturbed functioning of gluconeogenesis during day-time is also key to secure proton balance inside the cytosol. Since the plant mitochondrial pyruvate exporter remains unidentified, we explored potential mechanisms for mitochondrial pyruvate efflux *in silico* and postulate a pyruvate channel as the most efficient mechanism (Fig. 5). An increase in mATP synthase flux and re-export of mitochondrial protons to the cytosol at the cost of reducing power were observed when a pyruvate/H^+ symport and a pyruvate/H^+ antiport mechanism was active in the model respectively (Fig. 5b, c). We suggest a pyruvate/H^+ symport also thermodynamically unlikely as this should act against the proton gradient between the cytosol (pH 7.3) and mitochondrial matrix (pH 8.1) (Shen *et al*., 2013).

Acknowledgments

Funding was provided by the Research Fund KU Leuven. Figures were created with BioRender.com.

Competing Interests

None declared.

Author Contributions

JC and LJS designed the research; SD, SS, and NC performed research; SS and SD contributed new computational tools; all authors analyzed data; SD, SS, LJS, and JC wrote the paper; SD and SS created the figures. All authors revised the manuscript and approved the final version.

Data Availability

The authors declare that all data supporting the findings of this study are available within the paper and its supporting information files. The code required to reproduce the models and results in this paper are available on GitHub (https://github.com/stijndaems/Daems_et_al_CAM_2024).

References

Abraham PE, Hurtado Castano N, Cowan-Turner D, Barnes J, Poudel S, Hettich R, Flütsch S, Santelia D, Borland AM. **2020**. Peeling back the layers of crassulacean acid metabolism: functional differentiation between Kalanchoë fedtschenkoi epidermis and mesophyll proteomes. *The Plant Journal* **103**: 869–888.

Abraham PE, Yin H, Borland AM, Weighill D, Lim SD, De Paoli HC, Engle N, Jones PC, Agh R, Weston DJ, *et al.* 2016. Transcript, protein and metabolite temporal dynamics in the CAM plant Agave. *Nature Plants* **2**: 1–10.

Bartholomew DM, Rees DJG, Rambaut A, Smith JAC. **1996**. Isolation and sequence analysis of a cDNA encoding the c subunit of a vacuolar-type H+-ATPase from the CAM plant Kalanchoë daigremontiana. *Plant Molecular Biology* **31**: 435–442.

Borland AM, Barrera Zambrano VA, Ceusters J, Shorrock K. **2011**. The photosynthetic plasticity of crassulacean acid metabolism: an evolutionary innovation for sustainable productivity in a changing world. *New Phytologist* **191**: 619–633.

Borland AM, Griffiths H, Hartwell J, Smith JAC. **2009**. Exploiting the potential of plants with crassulacean acid metabolism for bioenergy production on marginal lands. *Journal of Experimental Botany* **60**: 2879–2896.

Brauner K, Birami B, Brauner HA, Heyer AG. **2018**. Diurnal periodicity of assimilate transport shapes resource allocation and whole-plant carbon balance. *The Plant Journal* **94**: 776–789.

Brilhaus D, Bräutigam A, Mettler-Altmann T, Winter K, Weber APM. **2016**. Reversible Burst of Transcriptional Changes during Induction of Crassulacean Acid Metabolism in Talinum triangulare. *Plant Physiology* **170**: 102–122.

Broetto F, Lüttge U, Ratajczak R. **2002**. Influence of light intensity and salt-treatment on mode of photosynthesis and enzymes of the antioxidative response system of Mesembryanthemum crystallinum. *Functional Plant Biology* **29**: 13–23.

Ceusters N, Borland AM, Ceusters J. **2021**. How to resolve the enigma of diurnal malate remobilisation from the vacuole in plants with crassulacean acid metabolism? *New Phytologist* **229**: 3116–3124.

Ceusters J, Borland AM, Londers E, Verdoodt V, Godts C, De Proft MP. **2008**. Diel Shifts in Carboxylation Pathway and Metabolite Dynamics in the CAM Bromeliad Aechmea ‘Maya’ in Response to Elevated CO2. *Annals of Botany* **102**: 389–397.

Ceusters J, Borland AM, Taybi T, Frans M, Godts C, De Proft MP. **2014**. Light quality modulates metabolic synchronization over the diel phases of crassulacean acid metabolism. *Journal of Experimental Botany* **65**: 3705–3714.

Ceusters N, Luca S, Feil R, Claes JE, Lunn JE, Van den Ende W, Ceusters J. **2019**. Hierarchical clustering reveals unique features in the diel dynamics of metabolites in the CAM orchid Phalaenopsis. *Journal of Experimental Botany* **70**: 3269–3281.

Cheung CYM, Poolman MG, Fell DavidA, Ratcliffe RG, Sweetlove LJ. **2014**. A Diel Flux Balance Model Captures Interactions between Light and Dark Metabolism during Day-Night Cycles in C3 and Crassulacean Acid Metabolism Leaves. *Plant Physiology* **165**: 917–929.

Chomthong M, Griffiths H. **2020**. Model approaches to advance crassulacean acid metabolism system integration. *The Plant Journal* **101**: 951–963.

Clark TJ, Guo L, Morgan J, Schwender J. **2020**. Modeling Plant Metabolism: From Network Reconstruction to Mechanistic Models. *Annual Review of Plant Biology* **71**: 303–326.

Cushman JC, Tillett RL, Wood JA, Branco JM, Schlauch KA. **2008**. Large-scale mRNA expression profiling in the common ice plant, Mesembryanthemum crystallinum, performing C3 photosynthesis and Crassulacean acid metabolism (CAM). *Journal of Experimental Botany* **59**: 1875–1894.

Davies DD. **1986**. The fine control of cytosolic pH. *Physiologia Plantarum* **67**: 702–706.

Dever LV, Boxall SF, Kneřová J, Hartwell J. **2015**. Transgenic Perturbation of the Decarboxylation Phase of Crassulacean Acid Metabolism Alters Physiology and Metabolism But Has Only a Small Effect on Growth. *Plant Physiology* **167**: 44–59.

Dittrich P. **1976**. Nicotinamide Adenine Dinucleotide-specific “Malic” Enzyme in Kalanchoë daigremontiana and Other Plants Exhibiting Crassulacean Acid Metabolism 1. *Plant Physiology* **57**: 310–314.

Dittrich P, Campbell WH, Black CC Jr. **1973**. Phosphoenolpyruvate Carboxykinase in Plants Exhibiting Crassulacean Acid Metabolism 1. *Plant Physiology* **52**: 357–361.

Ebrahim A, Lerman JA, Palsson BO, Hyduke DR. **2013**. COBRApy: COnstraints-Based Reconstruction and Analysis for Python. *BMC systems biology* **7**: 74.

Edwards GE, Foster JG, Winter K. **1982**. Activity and intracellular compartmentation of enzymes of carbon metabolism in CAM plants. In: Crassulacean acid metabolism: proceedings of the Fifth Annual Symposium in Botany (January 14-16, 1982)/edited by Irwin P. Ting and Martin Gibbs. Rockville, Md.: American Society of Plant Physiologists, c1982.

FELLE HH. **2005**. pH Regulation in Anoxic Plants. *Annals of Botany* **96**: 519–532.

Ferrari RC, Bittencourt PP, Rodrigues MA, Moreno-Villena JJ, Alves FRR, Gastaldi VD, Boxall SF, Dever LV, Demarco D, Andrade SCS, *et al.* 2020. C4 and crassulacean acid metabolism within a single leaf: deciphering key components behind a rare photosynthetic adaptation. *New Phytologist* **225**: 1699–1714.

Franco AC, Ball E, Lüttge U. **1990**. Patterns of gas exchange and organic acid oscillations in tropical trees of the genus Clusia. *Oecologia* **85**: 108–114.

Haferkamp I. **2007**. The diverse members of the mitochondrial carrier family in plants. *FEBS Letters* **581**: 2375–2379.

Hafke JB, Neff R, Hiitt MT, Liittge U, Thiel G. **2001**. Day-to-night variations of cytoplasmic pH in a crassulacean acid metabolism plant. *Protoplasma* **216**: 164–170.

Holtum J, Osmond C. **1981**. The Gluconeogenic Metabolism of Pyruvate During Deacidification in Plants With Crassulacean Acid Metabolism. *Functional Plant Biology* **8**: 31.

Holtum JAM, Smith JAC, Neuhaus HE, Holtum JAM, Smith JAC, Neuhaus HE. **2005**. Intracellular transport and pathways of carbon flow in plants with crassulacean acid metabolism. *Functional Plant Biology* **32**: 429–449.

Holtum JAM, Winter K. **1982**. Activity of enzymes of carbon metabolism during the induction of Crassulacean acid metabolism in Mesembryanthemum crystallinum L. *Planta* **155**: 8–16.

Jia F, Wan X, Zhu W, Sun D, Zheng C, Liu P, Huang J. **2015**. Overexpression of Mitochondrial Phosphate Transporter 3 Severely Hampers Plant Development through Regulating Mitochondrial Function in Arabidopsis. *PLOS ONE* **10**: e0129717.

Kaste JAM, Shachar-Hill Y. **2023**. Accurate flux predictions using tissue-specific gene expression in plant metabolic modeling. *Bioinformatics* **39**: btad186.

Kondo A, Nose A, Yuasa H, Ueno O. **2000**. Species variation in the intracellular localization of pyruvate, Pi dikinase in leaves of crassulacean-acid-metabolism plants: an immunogold electron-microscope study. *Planta* **210**: 611–621.

Kore-eda S, Noake C, Ohishi M, Ohnishi J, Cushman JC, Kore-eda S, Noake C, Ohishi M, Ohnishi J, Cushman JC. **2005**. Transcriptional profiles of organellar metabolite transporters during induction of crassulacean acid metabolism in Mesembryanthemum crystallinum. *Functional Plant Biology* **32**: 451–466.

Laloi M. **1999**. Plant mitochondrial carriers: an overview. *Cellular and Molecular Life Sciences CMLS* **56**: 918–944.

Le XH, Lee C-P, Millar AH. **2021**. The mitochondrial pyruvate carrier (MPC) complex mediates one of three pyruvate-supplying pathways that sustain Arabidopsis respiratory metabolism. *The Plant Cell* **33**: 2776–2793.

Le XH, Lee CP, Monachello D, Millar AH. **2022**. Metabolic evidence for distinct pyruvate pools inside plant mitochondria. *Nature Plants* **8**: 694–705.

Leverett A, Borland AM. **2023**. Elevated Nocturnal Respiratory Rates in the Mitochondria of CAM Plants: Current Knowledge and Unanswered Questions. *Annals of Botany*: mcad119.

Lewis NE, Nagarajan H, Palsson BO. **2012**. Constraining the metabolic genotype-phenotype relationship using a phylogeny of in silico methods. *Nature Reviews. Microbiology* **10**: 291–305.

Lüttge U, Smith JAC. **1984**. Mechanism of passive malic-acid efflux from vacuoles of the CAM plantKalanchoë daigremontiana. *The Journal of Membrane Biology* **81**: 149–158.

Lüttge U, Smith JAC, Marigo G. **1982**. Membrane transport, osmoregulation, and the control of CAM. In: Crassulacean Acid Metabolism. Rockville: American Society of Plant Physiologists, 69–91.

Mahadevan R, Schilling CH. **2003**. The effects of alternate optimal solutions in constraint-based genome-scale metabolic models. *Metabolic Engineering* **5**: 264–276.

Marigo G, Lüttge U, Andrew J, Smith C. **1983**. Cytoplasmic pH and the Control of Crassulacean Acid Metabolism. *Zeitschrift für Pflanzenphysiologie* **109**: 405–413.

de Mattos EA, LÜttge U. **2001**. Chlorophyll Fluorescence and Organic Acid Oscillations during Transition from CAM to C3-photosynthesis inClusia minor L. (Clusiaceae). *Annals of Botany* **88**: 457–463.

Maxwell K, Borland AM, Haslam RP, Helliker BR, Roberts A, Griffiths H. **1999**. Modulation of Rubisco Activity during the Diurnal Phases of the Crassulacean Acid Metabolism Plant Kalanchoë daigremontiana. *Plant Physiology* **121**: 849–856.

Millar AH, Heazlewood JL. **2003**. Genomic and proteomic analysis of mitochondrial carrier proteins in Arabidopsis. *Plant Physiology* **131**: 443–453.

Miszalski Z, Ślesak I, Niewiadomska E, Baczek-Kwinta R, Lüttge U, Ratajczak R. **1998**. Subcellular localization and stress responses of superoxide dismutase isoforms from leaves in the C3-CAM intermediate halophyte Mesembryanthemum crystallinum L. *Plant, Cell & Environment* **21**: 169–179.

Orth JD, Thiele I, Palsson BØ. **2010**. What is flux balance analysis? *Nature Biotechnology* **28**: 245–248.

Osmond CB. **1978**. Crassulacean Acid Metabolism: A Curiosity in Context. *Annual Review of Plant Physiology* **29**: 379–414.

Osmond CB, Holtum JAM, O'Leary MH, Roeske C, Wong OC, Summons RE, Avadhani PN. **1988**. Regulation of malic-acid metabolism in Crassulacean-acid-metabolism plants in the dark and light: In-vivo evidence from 13C-labeling patterns after 13CO2 fixation. *Planta* **175**: 184–192.

Ostrem JA, Vernon DM, Bohnert HJ. **1990**. Increased expression of a gene coding for NAD:glyceraldehyde-3-phosphate dehydrogenase during the transition from C3 photosynthesis to crassulacean acid metabolism in Mesembryanthemum crystallinum. *Journal of Biological Chemistry* **265**: 3497–3502.

Owen NA, Griffiths H. **2013**. A system dynamics model integrating physiology and biochemical regulation predicts extent of crassulacean acid metabolism (CAM) phases. *New Phytologist* **200**: 1116–1131.

Peckmann K, von Willert DJ, Martin CE, Herppich WB. **2012**. Mitochondrial respiration in ME-CAM, PEPCK-CAM, and C succulents: comparative operation of the cytochrome, alternative, and rotenone-resistant pathways. *Journal of Experimental Botany* **63**: 2909–2919.

Pratt RD, Ferreira GC, Pedersen PL. **1991**. Mitochondrial phosphate transport. Import of the H+/Pi symporter and role of the presequence. *Journal of Biological Chemistry* **266**: 1276–1280.

Roberts JK, Callis J, Wemmer D, Walbot V, Jardetzky O. **1984**. Mechanisms of cytoplasmic pH regulation in hypoxic maize root tips and its role in survival under hypoxia. *Proceedings of the National Academy of Sciences of the United States of America* **81**: 3379–3383.

Roberts JKM, Wemmer D, Ray PM, Jardetzky O. **1982**. Regulation of Cytoplasmic and Vacuolar pH in Maize Root Tips under Different Experimental Conditions 1. *Plant Physiology* **69**: 1344–1347.

Rona J-P, Pitman MG, Lüttge U, Ball E. **1980**. Electrochemical data on compartmentation into cell wall, cytoplasm, and vacuole of leaf cells in the CAM genusKalanchoë. *The Journal of Membrane Biology* **57**: 25–35.

Sakano K. **1998**. Revision of Biochemical pH-Stat: Involvement of Alternative Pathway Metabolisms. *Plant and Cell Physiology* **39**: 467–473.

Scheibe R. **2004**. Malate valves to balance cellular energy supply. *Physiologia Plantarum* **120**: 21–26.

Schöttler MA, Kirchhoff H, Weis E, Siebke K. **2002**. Metabolic control of photosynthetic electron transport in crassulacean acid metabolism-induced Mesembryanthemum crystallinum. *Functional Plant Biology* **29**: 697–705.

Shameer S, Baghalian K, Cheung CYM, Ratcliffe RG, Sweetlove LJ. **2018**. Computational analysis of the productivity potential of CAM. *Nature Plants* **4**: 165–171.

Shameer S, Wang Y, Bota P, Ratcliffe RG, Long SP, Sweetlove LJ. **2022**. A hybrid kinetic and constraint-based model of leaf metabolism allows predictions of metabolic fluxes in different environments. *The Plant Journal* **109**: 295–313.

Shen J, Zeng Y, Zhuang X, Sun L, Yao X, Pimpl P, Jiang L. **2013**. Organelle pH in the Arabidopsis endomembrane system. *Molecular Plant* **6**: 1419–1437.

Smith JAC, Bryce JH. **1992**. Metabolite compartmentation and transport in CAM plants. In: Tobin AK, ed. Society for Experimental Biology Seminar Series. Plant Organelles: Compartmentation of Metabolism in Photosynthetic Tissue. Cambridge: Cambridge University Press, 141–168.

Smith JAC, Heuer S. **1981**. Determination of the Volume of Intercellular Spaces in Leaves and Some Values for CAM Plants. *Annals of Botany* **48**: 915–917.

Stappen R, Krämer R. **1994**. Kinetic mechanism of phosphate/phosphate and phosphate/OH- antiports catalyzed by reconstituted phosphate carrier from beef heart mitochondria. *Journal of Biological Chemistry* **269**: 11240–11246.

Steudle E. **1980**. Water-relation Parameters of Individual Mesophyll Cells of the Crassulacean Acid Metabolism Plant Kalanchoë daigremontiana. *Plant Physiology* **66**: 1155–1163.

Sweetlove LJ, Ratcliffe RG. **2011**. Flux-balance modeling of plant metabolism. *Frontiers in Plant Science* **2**: 38.

Takabatake R, Hata S, Taniguchi M, Kouchi H, Sugiyama T, Izui K. **1999**. Isolation and characterization of cDNAs encoding mitochondrial phosphate transporters in soybean, maize, rice, and Arabidopis. *Plant Molecular Biology* **40**: 479–486.

Tay IYY, Odang KB, Cheung CYM. **2021**. Metabolic Modeling of the C3-CAM Continuum Revealed the Establishment of a Starch/Sugar-Malate Cycle in CAM Evolution. *Frontiers in Plant Science* **11**.

Töpfer N, Braam T, Shameer S, Ratcliffe RG, Sweetlove LJ. **2020**. Alternative Crassulacean Acid Metabolism Modes Provide Environment-Specific Water-Saving Benefits in a Leaf Metabolic Model. *The Plant Cell* **32**: 3689–3705.

Tsiantis MS, Bartholomew DM, Smith JAC. **1996**. Salt regulation of transcript levels for the c subunit of a leaf vacuolar H+-ATPase in the halophyte Mesembryanthemum crystallinum. *The Plant Journal* **9**: 729–736.

Wagner S, Steinbeck J, Fuchs P, Lichtenauer S, Elsässer M, Schippers JHM, Nietzel T, Ruberti C, Van Aken O, Meyer AJ, *et al.* 2019. Multiparametric real-time sensing of cytosolic physiology links hypoxia responses to mitochondrial electron transport. *New Phytologist* **224**: 1668–1684.

Wang Y, Smith JAC, Zhu X-G, Long SP. **2023**. Rethinking the potential productivity of crassulacean acid metabolism by integrating metabolic dynamics with shoot architecture, using the example of Agave tequilana. *New Phytologist* **239**: 2180–2196.

Williams TCR, Poolman MG, Howden AJM, Schwarzlander M, Fell DA, Ratcliffe RG, Sweetlove LJ. **2010**. A Genome-Scale Metabolic Model Accurately Predicts Fluxes in Central Carbon Metabolism under Stress Conditions. *Plant Physiology* **154**: 311–323.

Winter K, Foster JG, Edwards GE, Holtum JAM. **1982**. Intracellular Localization of Enzymes of Carbon Metabolism in Mesembryanthemum crystailinum Exhibiting C3 Photosynthetic Characteristics or Performing Crassulacean Acid Metabolism'. **69**.

Winter K, Smith JAC. **1996**. Crassulacean Acid Metabolism: Current Status and Perspectives. In: Winter K, Smith JAC, eds. Ecological Studies. Crassulacean Acid Metabolism: Biochemistry, Ecophysiology and Evolution. Berlin, Heidelberg: Springer, 389–426.

Winter K, Smith JAC. **2022**. CAM photosynthesis: the acid test. *New Phytologist* **233**: 599–609.

Yuan H, Cheung CYM, Hilbers PAJ, van Riel NAW. **2016**. Flux Balance Analysis of Plant Metabolism: The Effect of Biomass Composition and Model Structure on Model Predictions. *Frontiers in Plant Science* **7**.

Zhu W, Miao Q, Sun D, Yang G, Wu C, Huang J, Zheng C. **2012**. The mitochondrial phosphate transporters modulate plant responses to salt stress via affecting ATP and gibberellin metabolism in Arabidopsis thaliana. *PloS One* **7**: e43530.

Supporting Information

Fig. S1 Model prediction of diel CO_2 uptake compared to experimental data

Fig. S2 Model predictions of the diel course of key metabolites before applying metabolite accumulation constraints

Fig. S3 Comparison between diel model predictions and experimental data of key metabolites after applying metabolite accumulation constraints

Fig. S4 Comparison between temporal NAD-malic enzyme (ME) and NADP-ME activities during day-time in *Phalaenopsis* 'Edessa' and *Kalanchoë fedtschenkoi*

Fig. S5 Flux maps representing major nocturnal (P7-P12) proton-producing and proton-consuming reactions in the 12-phase ME-type CAM model

Fig. S6 Key cytosolic proton-producing and proton-consuming reactions during night-time in a ME-type CAM mesophyll cell

Fig. S7 Schematic representation of the ME- versus the PEPCK-CAM pathway

Fig. S8 Key cytosolic proton-producing and proton-consuming reactions during day-time and night-time in a PEPCK-type CAM mesophyll cell

Table S1 Experimental CO_2 exchange data from *Phalaenopsis* 'Edessa' leaves (Separate Excel file)

Table S2 Experimental diel metabolite data from the CAM orchid *Phalaenopsis* 'Edessa' (Separate Excel file)

Table S3 Experimental data used to determine a conversion factor fresh weight to unit surface area for *Phalaenopsis* 'Edessa' (Separate Excel file)

Table S4 General overview of constraints applied on the ME-type and PEPCK-type CAM models (Separate Excel file)

Table S5 Diurnal proton fluxes, relative to the cytosol, through PiC (proton-consuming) and vacuolar malate efflux (proton-producing)

Table S6 Lists containing pFBA output for all reactions during all temporal model phases for the ME-type CAM model with an active PiC and inhibited PiC (Separate Excel file)

Table S7 Sorted lists containing all cytosolic proton-producing and proton-consuming reactions during day-time and night-time for the ME-type CAM model (Separate Excel file)

Table S8 Sorted lists containing the five most significant cytosolic proton-producing and proton-consuming reactions during day-time and night-time for the ME-type CAM model (Separate Excel file)

Table S9 IDs and flux values of reactions that re-export protons from the mitochondrial matrix to the cytosol at the cost of reducing power when applying a pyruvate/proton antiport mechanism

Table S10 Sensitivity analysis: lists containing all cytosolic proton-producing and proton-consuming reactions during day-time and night-time for the ME-type CAM model at varying Vc/Vo ratios (Separate Excel file)

Table S11 Sensitivity analysis: lists containing all cytosolic proton-producing and proton-consuming reactions during day-time and night-time for the ME-type CAM model at varying maintenance costs (Separate Excel file)

Table S12 Sensitivity analysis: lists containing all cytosolic proton-producing and proton-consuming reactions during day-time and night-time for the ME-type CAM model at varying NAD-ME:NADP-ME ratios (Separate Excel file)

Table S13 Sensitivity analysis: lists containing all cytosolic proton-producing and proton-consuming reactions during day-time and night-time for the ME-type CAM model at varying cPPDK:pPPDK ratios (Separate Excel file)

Table S14 Sensitivity analysis: lists containing all cytosolic proton-producing and proton-consuming reactions during day-time and night-time for the PEPCK-type CAM model (Separate Excel file)

Table S15 Sensitivity analysis: lists containing the five most significant cytosolic proton-producing and proton-consuming reactions during day-time and night-time for the PEPCK-type CAM model (Separate Excel file)

Table S16 Sensitivity analysis: lists containing all cytosolic proton-producing and proton-consuming reactions during day-time and night-time for the ME-type and PEPCK-type co-decarboxylation CAM model (Separate Excel file)

Table S17 Sensitivity analysis: lists containing all cytosolic proton-producing and proton-consuming reactions during day-time and night-time for the ME-type sucrose-storing CAM model (Separate Excel file)

Table S18 Sensitivity analysis: lists containing all cytosolic proton-producing and proton-consuming reactions during day-time and night-time for the ME-type CAM model without (iso)citrate accumulation (Separate Excel file)

Table S19 Summary of the relative contribution of both PiC and GAPDH in diurnal cytosolic proton consumption over the range of tested modelling parameters

Table S20 Results of Flux Variability Analysis on some CAM-related and key proton reactions (Separate Excel file)

Methods S1 Extended Materials and Methods

Notes S1 Supplementary note associated with Fig. S5

Notes S2 Supplementary note associated with Fig. S6

Notes S3 Supplementary note associated with Fig. S7

Notes S4 Supplementary note associated with Fig. S8

Notes S5 Supplementary note associated with the sensitivity analyses (Tables S10-S18)